

# Disentangling magnetic and grain contrast in polycrystalline FeGe thin films using 4-D Lorentz Scanning Transmission Electron Microscopy

Kayla X. Nguyen<sup>1,2</sup>, Emrah Turgut<sup>2,3</sup>, Michael C. Cao<sup>2</sup>, Jack Glaser<sup>2</sup>, Zhen Chen<sup>2</sup>, Matthew J. Stolt<sup>4</sup>, Song Jin<sup>4</sup>, Gregory D. Fuchs<sup>2,5</sup>, David A. Muller<sup>2,5</sup>

1. *Department of Chemistry and Chemical Biology, Cornell University, Ithaca, NY 14853, USA*
2. *School of Applied and Engineering Physics, Cornell University, Ithaca, NY 14853, USA*
3. *Department of Physics, Oklahoma State University, Stillwater, OK 74078, USA*
4. *Department of Chemistry, University of Wisconsin–Madison, Madison, Wisconsin 53706, USA*
5. *Kavli Institute at Cornell for Nanoscale Science, Ithaca, NY 14853, USA*

## Abstract

The study of nanoscale chiral magnetic order in polycrystalline materials with a strong Dzyaloshinskii-Moriya interaction (DMI) is interesting for the observation of new magnetic phenomena at grain boundaries and interfaces. This is especially true for polycrystalline materials, which can be grown using scalable techniques and whose scalability is promising for future device applications. One such material is sputter-deposited B20 FeGe on Si, which has been actively investigated as the basis for low-power, high-density magnetic memory technology in a scalable material platform. Although conventional Lorentz electron microscopy provides the requisite spatial resolution to probe chiral magnetic textures in single-crystal FeGe, probing the magnetism of sputtered B20 FeGe is more challenging because the sub-micron crystal grains add confounding contrast. This is a more general problem for polycrystalline magnetic devices where scattering from grain boundaries tends to hide comparably weaker signals from magnetism. We address the challenge of disentangling magnetic and grain contrast by applying 4-dimensional Lorentz scanning transmission electron microscopy using an electron microscope pixel array detector. Supported by analytical and numerical models, we find that the most important parameter for imaging magnetic materials with polycrystalline grains is the ability for the detector to sustain large electron doses, where having a high-dynamic range detector becomes extremely important. From our experimental results on sputtered B20 FeGe on Si, we observe phase shifts of the magnetic helices as they thread through neighboring grains. We reproduce this effect using micromagnetic simulations by assuming that the grains have distinct orientation and magnetic chirality. We then compare spin textures of strained FeGe on a Si substrate to those on free-standing FeGe by performing electron energy loss spectroscopy and find that the helical phases are only present in free-standing FeGe. Our methodology for imaging magnetic textures is applicable to other thin-film magnets used for spintronics and memory applications, where an understanding of how magnetic order is accommodated in polycrystalline materials is important.

## I. Introduction

Power-efficient memory devices based on magnetic skyrmions in sputtered, polycrystalline thin films are increasingly promising[1-5]. Although the crystalline perfection afforded by the bulk synthesis of chiral magnetic materials has enabled new scientific understanding[6-8], applications

will require materials that are grown using scalable techniques such as sputtering. The chiral magnetism itself arises as a result of the Dzyaloshinskii-Moriya interaction (DMI)[9,10] that is present at specimen interfaces and in the volume of noncentrosymmetric materials with broken inversion symmetry. Here we focus our investigation on thin films of cubic B20 FeGe sputtered on Si. This material lacks crystalline inversion symmetry, however, in thin-film form, it is strongly modified by substrate-induced strain[11,12] relative to bulk crystals. Our work seeks to answer relevant questions including: how does the substrate-induced strain, sub-micron grain size and the presence of many grain boundaries alter the nanoscale chiral magnetism in this material? Imaging the noncollinear spin textures in these polycrystalline films is a direct approach to understanding questions relevant to applications.

Lorentz electron microscopy has been widely used to investigate the real space magnetization profiles of chiral and topological spin textures, e.g. helices and magnetic skyrmions [13]. One such technique, Lorentz transmission electron microscopy (LTEM), provides nanometer spatial resolution; however, the electron beam must be defocused to obtain magnetic contrast causing strong Fresnel fringes at the grain boundaries and obscuring magnetic information [6,14-17]. Lorentz scanning transmission electron microscopy (LSTEM) presents an alternative [18,19] in the form of differential phase contrast (DPC) imaging, which uses a focused electron beam thus avoiding information delocalization. DPC imaging measures the deflection of a focused electron beam due to the electromagnetic field within the sample, which enables the study of the internal structure of magnetic skyrmions [20,21]. However, there are multiple constraints to DPC imaging including: (1) limited dynamic range of the detector limits the sensitivity to detect the extremely small magnetic fields that are expected in modern devices, (2) nonlinearities introduced by the signal normalization when the detector is not perfectly centered, and (3) changing beam shape due to electron channeling, which gives rise to contrast reversals as the electron beam moves through the sample [22-24]. As a result, experiments using both LTEM and DPC have mostly focused on single-crystal samples that exhibit sparse grains and few defects, thus presenting a structurally uniform medium for imaging.

Here, we use a version of LSTEM known as 4-dimensional Lorentz scanning transmission electron microscopy (4-D LSTEM) with an electron microscope pixel array detector (EMPAD) [25]. This technique can sense electromagnetic beam deflections by acquiring electron diffraction patterns at every  $x$ - $y$  scan position with a high  $k_x$ - $k_y$  momentum resolution. From the electron diffraction pattern, a center of mass (COM) signal can be extracted and used to quantitatively reconstruct the sample's magnetic field [24]. The key advantage of the EMPAD is its high dynamic range, which enables sensitive mapping of magnetic fields,  $(\mu T / \sqrt{Hz})$ , and captures simultaneously the crystalline and magnetic information without saturating the detector. From this, we distinguish magnetic field information from crystalline grain structure effects and probe each effect independently. In the following sections, we (1) highlight the fundamental ideas behind detection of magnetic fields with high sensitivity, (2) show that the precision relies on the number of electrons a detector can sustain, stressing the importance of a high-dynamic-range and high-speed detector, and (3) demonstrate our technical approach to disentangling magnetic signal from the signal due to grain contrast. Using this approach, we observe changes in the magnetic textures from the different DMI between adjacent grains, which we find only in regions of free-standing FeGe.

## II. Deflection of the Electron Beam due to Magnetic Fields

To detect a magnetic field in Lorentz Microscopy, we consider a parallel electron beam source that is incident perpendicular to the plane of the specimen, along the z-axis. Here, we ignore stray field effects, which gives rise to an unmeasurable z-component deflection and consider only the deflections due to the in-plane magnetic field[26,27]. The equation for the electron beam deflection is then given as:

$$\beta(x) = \frac{e\lambda B_0 t}{h}, \quad (1)$$

where  $B_0$  is the local magnetic field,  $e$  is the electron charge,  $\lambda$  is the wavelength of the electron beam,  $t$  is the sample thickness and  $h$  is Planck's constant. This deflection of the electron beam,  $\beta$ , can be measured by tracking the COM of the diffraction pattern as we scan the electron beam, which is related to the local magnetic field.

The argument above presents the classical treatment of the electron beam deflection in a magnetic field. On the length scale of electron microscopy, electron-specimen interactions and the beam shape should also be treated quantum mechanically. For elastic scattering, the deflection of the electron beam by the local magnetic field is the change in momentum of the electron wave function,  $\langle \vec{p} \rangle$  [24], which is the COM signal in our diffraction pattern. Using Ehrenfest's theorem[28], the expectation value of the Lorentz force in terms of  $\langle \vec{p} \rangle$  is [24] ,

$$\frac{d\langle \vec{p} \rangle}{dt} = \langle [\hat{H}, \hat{p}] \rangle = \langle e(\vec{E} + \vec{v} \times \vec{B}) \rangle \quad (2)$$

where  $\hat{H}$  is the Hamiltonian,  $e$  is the charge of the electron,  $\vec{E}$  is the electric field,  $\vec{v}$  is the velocity at which the electron is traveling and  $\vec{B}$  the magnetic field. Again, for elastic scattering the velocity remains constant so the rate of change of momentum with time can be mapped to the rate of change of momentum with thickness into the sample. This  $\langle \vec{p} \rangle$  can be extracted from the intensity of the scattered wave function,  $\Psi$ , as:

$$\langle \vec{p} \rangle = \int \Psi^*(\vec{p}) \hat{p} \Psi(\vec{p}) d\vec{p} = \int \hat{p} |\Psi(\vec{p})|^2 d\vec{p} = \int \hat{p} I(\vec{p}) d\vec{p} \quad (3)$$

where  $I$  is the intensity of the diffraction pattern and  $\hat{p}$  is the momentum operator. From equations 2 and 3, a shift in  $\langle \vec{p} \rangle$  is perpendicular to the magnetic field and parallel to the electric field. Rewriting  $\langle \vec{p} \rangle$  in real space, we see that it is also the probability current flow,  $\langle \vec{j} \rangle$ , where the expectation value for  $\langle \vec{j} \rangle$  is calculated for an evolving electron wave function, changing as it propagates through the specimen[20]:

$$\langle \vec{p} \rangle = \frac{\hbar}{2i} \int [\Psi^*(\vec{r}, \vec{r}_p) \vec{\nabla} \Psi(\vec{r}, \vec{r}_p) - \Psi(\vec{r}, \vec{r}_p) \vec{\nabla} \Psi^*(\vec{r}, \vec{r}_p)] d\vec{r} = 2m\langle \vec{j} \rangle \quad (4).$$

Here,  $r$  is the real space position at an arbitrary point.  $r_p$  is the position of the probe in real space, and  $m$  is the mass of the electron. Although the equations above give us a direct relation for  $\langle \vec{p} \rangle$  to the electromagnetic field, every signal from  $\langle \vec{p} \rangle$  results in a signal with contributions from the nuclear, core, valence and external electric and magnetic fields. Disentangling these contributions based on their different spatial distributions is discussed in section V. Equations (2)-(4) describe

the fundamental physics used when determining electromagnetic fields from a deflection of the electron beam. In order to experimentally quantify the parameters that affect our signal sensitivity, we develop a framework to model and predict the sensitivity based on the parameters we can optimize in the electron microscope.

### III. Determining Magnetic Field Detection Sensitivity

The magnetic field sensitivity that we can obtain using COM imaging depends on how well we can track the deflection of the electron beam. To quantify this, we first present an analytical approach to determine the sensitivity of the magnetic field based on a model previously described by Chapman et al [26] (Appendix A). Here, Fig. 1 shows a schematic of a split detector from which the shift of scattered electron beam due to a magnetic field in the sample is detected[26].

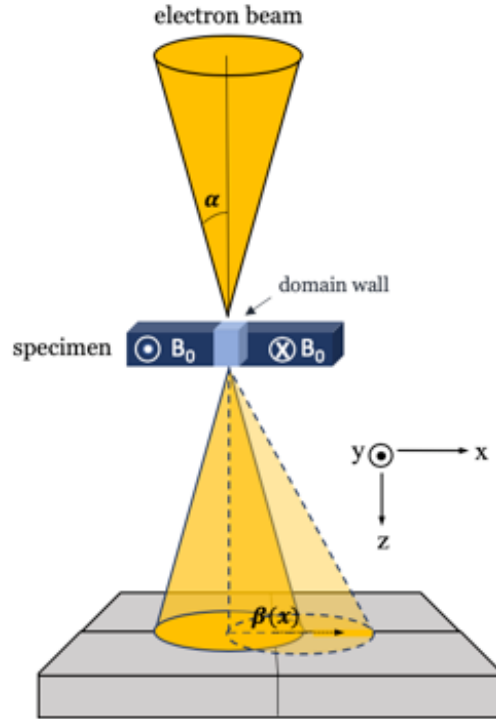


FIG. 1. Schematic of signal deflection for a split detector used in LSTEM, where we show change in the angular deflection of the electron beam due to the change in the Lorentz force as it is moved from the left to right domain.

Here, the sensitivity of COM has two dependencies: (1)  $\alpha$ , the semi-convergence angle of the electron beam, which provides the limit in spatial resolution, and (2)  $n$ , the number of electrons or dose of the electron beam, which tells you how many electrons are needed to sustain a signal that is adequately above Poisson noise. These two variables are parameters that can be easily adjusted in the electron microscope. Using the analytical model in Appendix A, we observe the minimum deflection  $\beta_L$  as:

$$\beta_L = \frac{\pi\alpha}{4\sqrt{n}} \quad (5).$$

In this analytical model, we only show how deflection sensitivity, hence field sensitivity, is

dependent on a split detector or a detector with two pixels. In order to calculate the field sensitivity of a detector with more than two pixels, we move from an analytical to a numerical model to investigate how deflection sensitivity is affected by  $n$ , the number of electrons that we use in our electron beam, and  $\vec{v}$ , the number of pixels in our detector described in Appendix B. Doing so, we answer the question, do more pixels in a detector lead to an improved detection sensitivity to fields?

In our numerical model, we assume a one-dimensional detector that is entirely illuminated by an electron beam represented as a Gaussian distribution with varying Poisson noise. Here, we vary the number of pixels in our detector, the number of electrons used in our electron beam, and hence the Poisson noise. We then calculate the COM of the electron beam on the detector with over 2000 samples with random varying Poisson noise to find the standard deviation of the COM measurements from each sample. The standard deviation that we obtain is the error in our COM measurement, related to how precisely we can extract the COM. By multiplying the standard deviation with a semi-convergence angle,  $\alpha$ , we can relate this standard deviation to the minimum deflection angle of our electron beam,  $\beta$ . In our numerical model, we choose  $\alpha$  to be 200  $\mu\text{rad}$  because it corresponds to a spatial resolution of 7.6 nanometers for a 200 kV electron beam, typical of the resolution needed to image magnetic skyrmions in single crystal FeGe. From Fig. 2(a), we find that our deflection,  $\beta$ , is strongly dependent on the total number of electrons, and only weakly on the number of pixels in our detector, with diminishing returns once more than 10 pixels per disk are added.

In order to convert  $\beta$  to the magnetic field, we use beam energy of 200 keV and a sample thickness of 100 nm [Fig. 2(b)]. Here, our results show that if we want to observe magnetic fields with sensitivity less than 1 milliTesla (mT), the number of electrons must be greater than 1 million. From Fig. 2(a) and 2(b), we find that a detector with high dynamic range detector is more important for signal sensitivity than a detector with more pixels. Traditional arguments for detectors with many pixels emphasize the importance of angular resolution, where more pixels in the detector would give higher sensitivity in deflection detection. Here, we show through our models that this is not necessarily the case for COM measurements. We observe that even with many pixels, deflection sensitivity is still limited if a detector cannot collect or sustain a high number of electrons integrated over all channels. While there is diminishing return in improving the SNR with an increased number of pixels, for detectors with poor dynamic range, there sometimes might be a benefit to spreading the total dose over more pixels to avoid saturation, provided the dose/pixel is much larger than the readout noise per pixel. In summary, we find that we do not need many pixels on our detector to detect small fields. Instead, the most important thing is the ability of a detector to handle large total doses; here, dose/pixel becomes important. For detecting very small deflections or fields, dynamic range is the limiting factor.

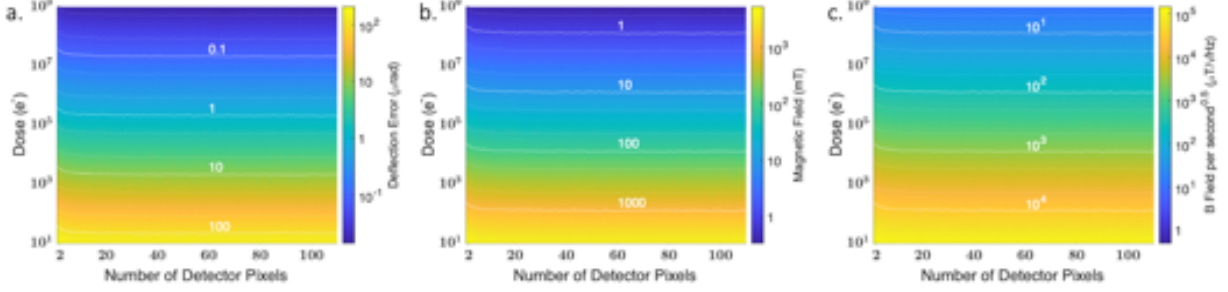


FIG. 2. Numerical simulations showing (a) the minimum measurable deflection, (b) smallest measurable magnetic field, given for  $n$  electrons and  $\vec{v}$  pixels, and (c) the dependence of magnetic field sensitivity and acquisition speed in terms of  $\frac{\mu T}{\sqrt{Hz}}$ . Here, the solid lines represent their respective signal as  $10^n$ , the first dotted line below the solid line is  $0.5 \times 10^n$ , and the second dotted line is  $0.2 \times 10^n$ . From our plots, we observe that field resolution is more dependent on the number of electrons than the number of pixels on a detector, with diminishing returns beyond 10 pixels.

To measure these small deflections with high precision experimentally, we need cameras with higher dynamic ranges and faster read-out speeds than was possible with scintillator-based technologies. The EMPAD presents one such a solution[25]. Compared to traditional diffraction detectors such as CCDs, the EMPAD has fast acquisition at 0.86 ms per frame and a high dynamic range of 30 bits; this means that the EMPAD can detect one to one million electrons without detector saturation at high signal to noise. Using the EMPAD, COM can achieve a comparable sensitivity to the high sensitivity magnetic detection techniques, such as NV centers and SQUID imaging [29]. For instance, extreme field sensitivity,  $< 1 \frac{\mu T}{\sqrt{Hz}}$ , can be obtained if we acquire diffraction patterns at  $\sim 50$  ms per frame and 1nA beam current [Fig. 2(c)]. For a typical field emission source and a 0.3 mrad aperture semiangle, this will result in a spatial resolution of 5-7 nm at this sensitivity. Reducing the dwell time to 5 ms and increasing the aperture size to 0.6 mrad gives a spatial resolution of  $\sim 3$  nm, and a sensitivity of  $\sim 20 \frac{\mu T}{\sqrt{Hz}}$ . Here, using simulations, we have analyzed how to optimize the detection of extremely small magnetic field variations in the electron microscope, highlighting the importance of a high-dynamic range and high-speed diffraction detector such as the EMPAD.

#### IV. Experimental Results

In this section, we apply 4-D LSTEM to study bulk single-crystal FeGe, a well-characterized material system [6,14,30-32], before proceeding to our investigation of polycrystalline materials in section V. The quantitative comparison to a known material allows us to test the accuracy and precision of the LSTEM measurements. The sample preparation of single crystal FeGe was discussed previously in [33-36]. Samples are prepared using a focused ion beam and subsequently imaged at 300 keV with a 230 micro radian semi-convergence angle on an FEI-Titan. The sample was cooled to 240 K using a Gatan cryo-holder and imaged under at 130 mT field perpendicular to the sample plane. During scanning we record the full convergent beam electron diffraction (CBED) pattern at high-dynamic range and high speed [Fig. 3(a)]. The CBED pattern contains all of the magnetic and crystallographic information, including the Lorentz force, which is extracted

from the beam COM. The sample's magnetic induction field for the x and y direction are shown in Fig. 3(b) and (c), respectively. Using Fig. 3(b) and (c), we reconstruct the magnetic field magnitude, which shows the skyrmion lattice [Fig. 3(d)]. Our in-focus 4-D LSTEM image of the skyrmion lattice agrees quantitatively with prior measurements using LTEM[14] and DPC[20].

To estimate the noise in our measurements, we take a line profile of the magnetic field in Fig. 3(c) and perform a fit to our line. Here, we obtain the root mean square (RMS) error by measuring the deviations in the line profile of the magnetic field compared to our fit [Fig. 3(e)]. We find a root mean squared (RMS) error of 3.6 mT and observe that we indeed have mT sensitivity in field.

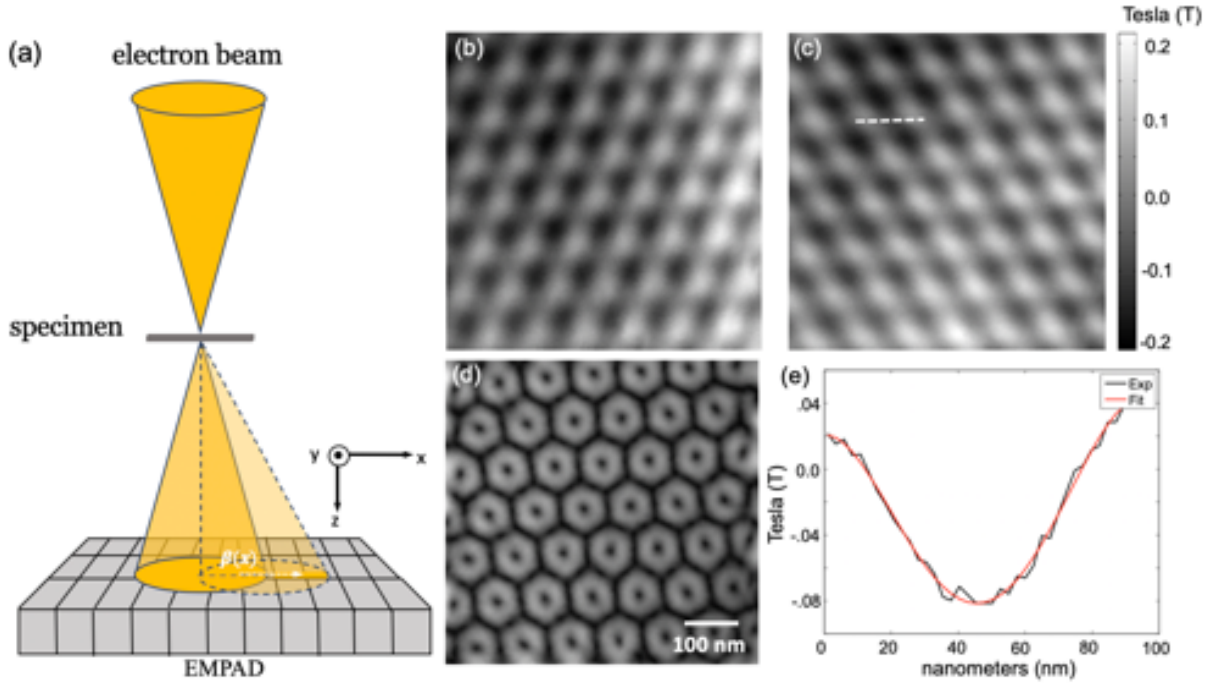


FIG. 3. (a) Schematic of magnetic imaging with EMPAD in Lorentz-STEM mode. We capture the full scattered distribution in momentum space with the EMPAD at every scan position, from which we can also reconstruct the magnetic field components in the (b) x and (c) y directions (in units of Tesla). From (b) and (c), we obtain (d) the magnitude of the skyrmion field. We record a line profile from the magnetic field deflection in y (c), and we compare it to its fit (e). Here, we observed a root mean square (RMS) of 3.6 mT. White scale bar in (d) also applies to panels (b) and (c).

Aside from magnetic fields, the 4-D LSTEM with the EMPAD also simultaneously provides the information needed to generate images that are usually obtained from conventional techniques such as annular dark field, bright field, and specialized techniques such as quantitative measurements of thickness, strain, tilt, polarity, atomic fields, and the long-range electric fields. Although we can detect sensitive magnetic fields, crystallographic scattering effects could dominate signals from real specimens, leading to artifacts or misinterpretation of magnetic signals. For spintronic devices, magnetic specimens are typically sputtered as thin films where grain sizes range from a couple of nanometers to microns. One such material is sputter-deposited B20 FeGe

on Si [11,37-40]. Probing the magnetism of sputtered B20 FeGe is extremely challenging because the sub-micron crystal grains exist on the same length scale as the characteristic length scale of the magnetic texture. Therefore, disentangling magnetic effects from grain contrast is extremely important. We present an approach to disentangle the signal of magnetic contrast from grain contrast, allowing each to be probed independently. This is enabled by the high dynamic range of the EMPAD, where multiple imaging modes can be used to extract and separate the two signals.

## V. Disentangling grain and magnetic contrast

As a starting point, we must first consider how electron scattering is affected when both magnetic and grain contrast are present. Previously, Chapman et al. [41] showed that by using an annular quadrant detector instead of a solid quadrant detector, the unwanted grain contrast could be reduced and a smoother magnetic contrast could be obtained by narrowing the collection angles of the detector. Kohl et al. [42] discussed how using only a narrow range of annular cut-off angles relative to the direct electron beam acts as a low-pass filter for the image. Krajnak et al. [43] showed that magnetic contrast can also be enhanced by tracking only the edge of the bright field disk, which also serves to suppress high-spatial-frequency, non-magnetic features in very fine grain materials. This can be understood in terms of Kohl et al.'s [42] analysis by recognizing that magnetic field signals are enhanced due to their slowly-varying long-range potentials. Diffraction contrast from grains and grain boundaries, on the other hand, are encoded as short-range potentials, where this signal can be smaller than the probe size for a large electron beam [44]. Cao et al. [44] explored the asymptotic limits for long-range potentials where the potential varies slowly across the probe shape, and short-range potentials where the potential is much smaller than the probe size, showing how their signals are distributed differently in momentum space. For magnetic imaging, where the probe is a few nanometers in size, magnetic fields are long-range with respect to the probe, and changes in grain contrast are short range.

In particular, a short-range potential, such as a grain boundary, changes the intensity distribution inside the bright field disk but it does not deflect the disk boundaries. A long-range potential, such as a magnetic field in a ferromagnet, uniformly shifts the entire bright field disk similar to the classical analysis of Ref. [26]. These different angular distributions are difficult to track with only a quadrant detector. A key aspect of this angular-separation technique is having a sufficient number of pixels on the detector to separate these two signals and still be able to record sufficient signal from diffracted beams to track grain orientation simultaneously.

We study B20 FeGe (176 nm thickness) films sputtered on Si to test how the intensity distribution signal changes in the diffraction pattern using the full 128x128 pixels on the EMPAD and its high dynamic range. We polished our sample in plan-view using a 1- 3 degrees polishing angle to remove the Si region at the tip of the sample, exposing a thin wedge of free-standing FeGe. Then we use the FEI-Tecna F20 at 200 keV with a Gatan double-tilt cryo-cooling holder to image our sample at 100 K in 4-D LSTEM mode with the EMPAD, where we collect a diffraction pattern at each scan position. We do not use the main objective lens for focusing because it induces a 2 T field to the sample, which would fully saturate its magnetization and erase all chiral magnetic texture. Instead, we use the condenser lenses to focus the probe and we use the objective and condenser mini lenses to either null the field on the sample or add a small external



vertical field. We also use a semi-convergence angle of  $615\ \mu\text{rad}$ , from which a spatial resolution of  $2.5\ \text{nm}$  is recovered.

We observe magnetic helices in the sputtered B20 FeGe within different grains by 4-D STEM. We will return to the significance of this finding at the end of Sec. IV, but first we discuss the details of the measurement. To decouple the magnetic field from grain contrast, we vary a virtual aperture on our diffraction pattern and for each aperture, we extract a COM signal, where the sampled angular distribution of the scattered electron beam is limited by the aperture sizes shown Fig. 4(a)-(d). When the size of the aperture is less than the size of the incident diffracted disk, we treat the COM signal as coming from only the short-range potentials such as grain boundaries in the sample. When the aperture is larger than the size of the incident beam, we treat the signal as coming from both the long-range field (magnetic field) and the diffracted beams (grain structure). Here, we choose aperture sizes of  $180\ \mu\text{rad}$ ,  $430\ \mu\text{rad}$ ,  $700\ \mu\text{rad}$  and  $4.6\ \text{mrad}$  [Fig. 4(a)-(d)], which correspond to the radii of the apertures. When the aperture sizes are smaller than our semi-convergence angle,  $615\ \mu\text{rad}$  [Fig. 4(a)-(b)], we find that the signal only comes from the short-range potentials, i.e. the grain contrast, and the signal for the magnetic field is not observed [Fig. 4(e)-(f)]. When we increase our aperture size to  $700\ \mu\text{rad}$  [Fig. 4(c)], which is slightly larger than our semi-convergence angle, we observe a signal from the magnetic field [Fig. 4(g)]. When we extend our aperture size further to  $4.6\ \text{mrad}$  [Fig. 4(d)], we observe both the signal for the magnetic field and grain contrast [Fig. 4(h)], similar to Fig. 4(g); however, the signal here is dominated by thermal diffuse scattering (including Kikuchi bands), making the signal of the magnetic field less sharp than Fig. 4(g). The optimal angular distribution range for magnetic imaging comes from choosing an aperture angle that is slightly larger than our semi-convergence angle [41].

By calculating the COM for different aperture sizes, we use the fact that atomic potentials or grain effects are short-range potentials, which appears when our aperture is smaller than our incident disk; here, there are no magnetic contributions (i.e. the magnetic vector potential varies slowly over these small distances). On the other hand, long range-potentials such as those due to the magnetic field cause the entire diffracted disk to shift; these effects best seen when the aperture annulus is matched to edge of the incident disk. We exploit this fact by subtracting Fig. 4(f), which is the COM image when the aperture is slightly smaller than the incident disk, from Fig. 4(g), which is the COM image when the aperture is slightly larger than the incident disk, to make Fig. 4(i), where the magnetic contributions are enhanced compared to grain contrast. In Fig. 4(i), the reason why the magnetic field contributions appear magnified is because most of the atomic, grain contrast distribution has been subtracted away. To compare Fig. 4(i), the magnetic field contribution to an image of only grain contrast, we used Fig. 4(j) to show only grain contrast in false color. We get our image for only the grain contrast by subtracting Fig. 4(g) from Fig. 4(h), this method subtracts away the magnetic contributions and leave only the grain contributions, seen in Fig. 4(j). In addition, we also observe changes due to the electrostatic potential; here, the yellow contrast in Fig. 4(i) comes from the thickness gradient of a wedge sample, which can be recovered from the electrostatic potential. From our results in Fig. 4, we show that we can measure the helical phases by measuring the long-range potential shifts due to the magnetic field [Fig. 4(i)]. Although changes in the electric fields are present in the diffraction signal, it does not affect the magnetic signal. It should be pointed out that accurate decoupling of different contributions to the

COM images relies on a good understanding of how each signal is reconstructed. By exploring the short and long-range potentials as intensity distributions in our diffraction pattern, we can enhance the signal for magnetic fields [Fig. 4(i)] and decouple it from the grain structures [Fig. 4(j)].

Having established a method to resolve nanoscale magnetic contrast in the presence of structural disorder, we now discuss our observations of magnetic helices. The orientation of helical magnetic states can be defined in terms of a Q-vector – the vector about which the magnetic moment spirals as a function of position. Thin-film FeGe (and other B20 magnetic materials) samples typically exhibit a helical state with a Q-vector oriented out-of-plane, which has been verified by both neutron scattering experiments [12][10] and by the ferromagnetic resonance of the helical state [11][9]

. This tendency can be attributed to substrate-induced tensile strain in the film which produces anisotropy oriented in the sample plane [11,20,45-48], consistent with strain-dependent experiments in single-crystal FeGe samples [46].

To see helices in an electron microscopy experiment, the Q-vector must lie in the plane. In the case of out-of-plane Q-vectors, the magnetization always remains in the sample plane as it spirals about the out-of-plane direction. Therefore, any deflection acquired by the electron beam as it passes through the upper part of the film will be compensated by a deflection in the opposite direction in the lower part of the film. In contrast, when the Q-vector lies in the plane, the beam deflections are not canceled, and they vary with the lateral position leading to the stripe-like pattern seen in Fig. 4. This both offers an opportunity to study the helical texture as it threads through different crystalline grains and it is surprising because it shows that this material is not obviously under tensile strain. These topics are addressed in Sec. V.

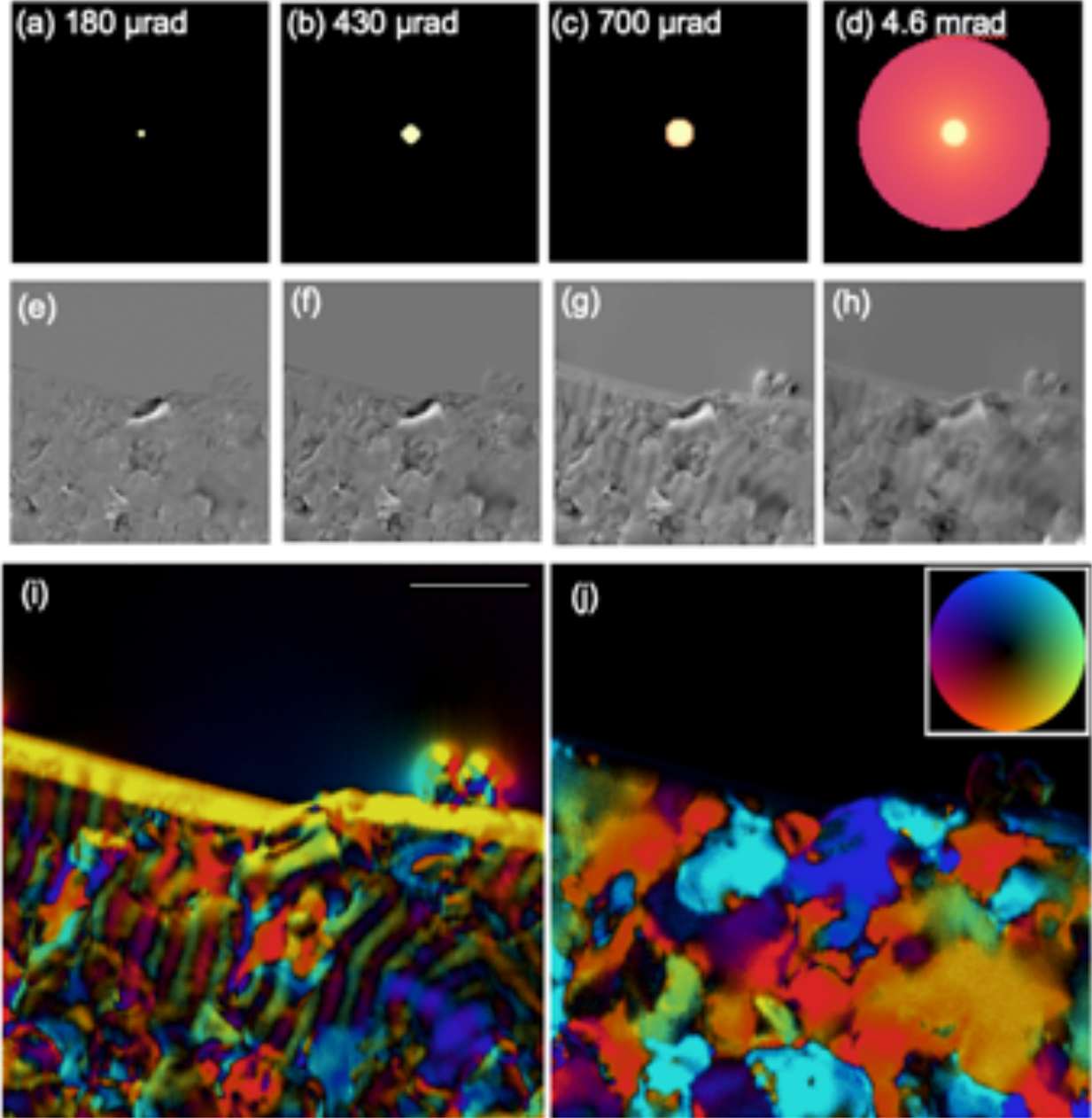


FIG. 4. Optimizing magnetic field contrast by varying the aperture size. Here we calculate the COM in the x-direction, using with aperture sizes of (a) 180  $\mu\text{rad}$  (b) 430  $\mu\text{rad}$  (c) 700  $\mu\text{rad}$  and (d) 4.6 mrad. Figures (e) – (h) show the x-component of the COM images corresponding to apertures (a) – (d). By exploiting the long-range potential due to the magnetic field, we use (g), which corresponds to an aperture just larger than the incident disk (c), we subtract it from (f), which corresponds to an aperture just smaller than the incident disk. Doing so, we can extract (i) the magnetic field from grain contrast, where grain contrast contributions have been reduced (Relative magnitude and direction of field are indicated by the color wheel in (j)). The false colored vector map in (j) shows only grain contrast image (as a tilt of the Ewald Sphere), which we get by subtracting COM image (g) from (h), here; the magnetic contributions are subtracted away leaving only contributions from short-range atomic potential i.e. the grains. White scale bar in (i) is 200 nm.

## VI. Helical Magnetic Phases at Grain Boundaries

The ability to image structural features and magnetic effects at the same time has enabled us to study how the helical vectors change along the boundaries of individual FeGe grains. For chiral magnets made from thin film sputtering, grain contrast and substrate effects have limited direct imaging of these chiral magnets, such as the helical phases, due to image distortions caused by Fresnel fringes in Lorentz-TEM, where artifacts arising from grain contrast could be misinterpreted for magnetic effects [15-17,43]. In addition, structural effects from the grains in B20 FeGe were previously shown by electron back scattering diffraction (EBSD) to be twinned, which causes switching of crystal chirality [11], adding another layer of difficulty when decoupling magnetic from grain effects. Therefore, to decouple all of these effects and observe the intrinsic magnetic properties of the B20 FeGe magnets, we utilize 4-D LSTEM with the EMPAD. From the diffraction patterns collected, we measure the COM of varying aperture sizes [described in the section above and shown in Fig. 4] to decouple magnetic effects from grain effects in the same data set. Here we look closely into how helical phases change as they thread through adjacent grains.

We first reconstruct a dark field image [Fig. 5(a)] of the top leftmost spot in our diffraction pattern [Fig. 5(c)] to distinguish individual grains from one another. Then by calculating the COM with different aperture sizes, we observe a shift in the phase of the helical vectors as it moves through adjacent grains. From our magnetic field results, we see a color change going from red to yellow and vice versa at the grain boundary of grain [c] and grain [d] in Fig. 5(b), essentially a  $\pi$ -phase shift in the helices as they cross the boundary. The diffraction pattern of Fig 5(c) shows the highlighted grain is tilted a few degrees off the [110] zone with the (300) spot most strongly excited in the top leftmost corner – this is the spot used for forming the darkfield image. Two weaker {111} spots point in the direction of the lowermost grain boundary, suggesting this boundary is close to a (111) face of grain [c]. The face to its immediate right would then be a (100) type face. As with our previous electron backscatter diffraction measurements[11], the adjacent grains most seem to follow a mostly (111) texture with in-plane rotation, here tilted several degrees off this zone based on the Kikuchi bands in Fig. 5(d). Grains c and d seem to share at least one common low-order Kikuchi band, consistent with the preservation of the helical stripe direction in the vertical direction of the image.

As a resolution test, when we take the line profile of the grain [c] in Fig. 5(a), we find from our 25-75% test [49] that we have a spatial resolution of 4.1 nm [Fig. 5(e)]. This width includes the tilt of the grain boundary to the film normal, so should be viewed as an upper bound. For instance, a tilt of 1 degree would provide an additional  $\sim 2$  nm of broadening for a 100-nm-thick region of the film.

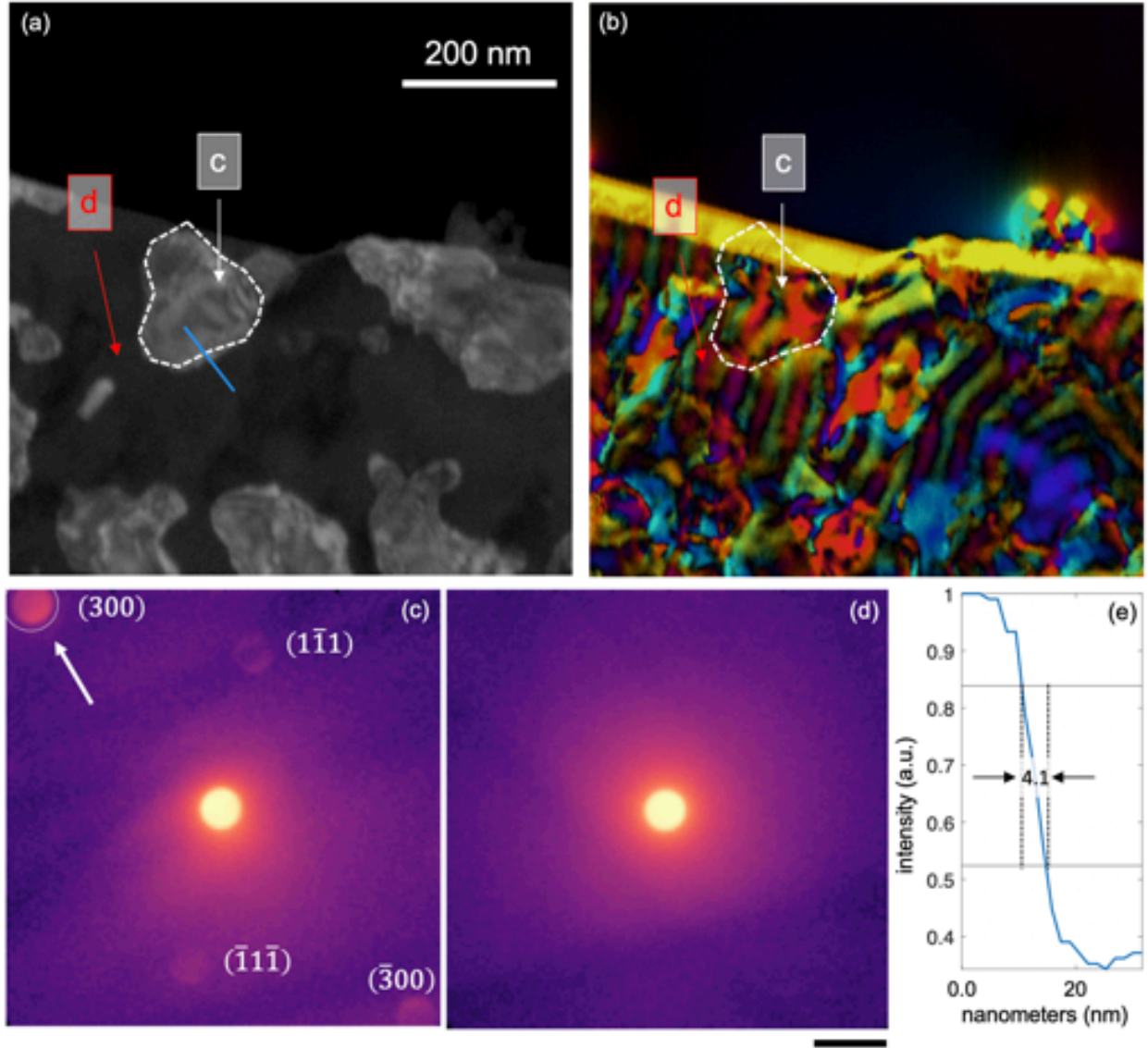


FIG. 5. By analyzing the grain orientations shown in the dark field image in (a) and we relate it to the magnetic field image in (b). From which, we observed that adjacent grains [c] and [d] have a generalized grain orientation, corresponding to an in-plane rotation. In addition, we observed a shift in helical vectors as it moves across the grain [c] and [d]. We chose the top left spot in (c) to form our dark field image in (a). Black scale bar under (d) represents 1.8 milliradians. (e) Blue line profile of across the boundary of grain [c] in panel (a) shows a 4.1 nm edge resolution when we perform a 25-70% resolution test. This is an upper bound as it neglects the projected mistilt of the grain.

The shift of phase in the helices as they cross the (111) grain boundary plane suggests a shift in chirality. To test this hypothesis, we investigate the effects of grains on the helical configuration by performing micromagnetic simulations with Mumax3 [50]. We first randomly generate grains with 320 nm average size using Voronoi tessellation[50] [Fig. 6(a)]. Next, we randomly assign either positive or negative DMI coefficients to these grains as shown in Fig. 6(b).

From magnetometry measurements, we confirm that our films have a small easy-plane uniaxial anisotropy,  $K_u$ , approximately  $-3500 \text{ J/m}^3$  [6,11]. We note that the  $K_u$  of the sample may be altered in the process of preparing it for 4-D LSTEM due to mechanical polishing and thickness variation.

To account for this effect, we vary  $K_u$  between 0 and  $-3000 \text{ J/m}^3$  in our simulations and obtained a very similar spin configuration. In Fig 6, we show the simulation for  $K_u = -3000 \text{ J/m}^3$ . Particularly, we start the simulation by initializing the system into a random magnetic configuration and allow it to micromagnetically relax to its ground state. The spin configuration of this ground state is shown in Fig. 6(c) as color-coded for the magnetization direction. We notice that the helical vectors shift at the grain boundaries by a half pitch when DMI sign changes, which agrees with our 4-D LSTEM observation. Therefore, we conclude that for FeGe on Si(111), the crystal grain orientation couples to the crystal chirality, and thus to the DMI.

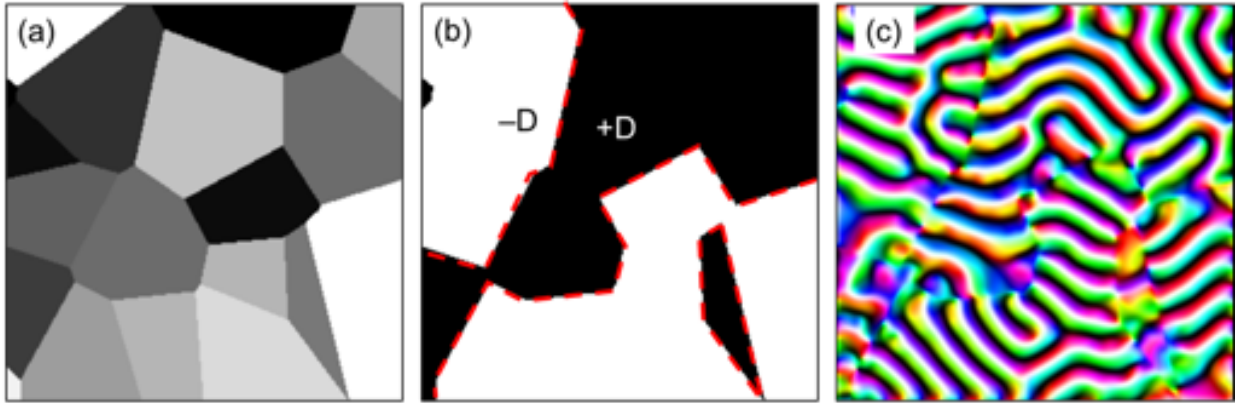


FIG. 6. Micromagnetic simulations of disordered medium of FeGe thin films. (a) Randomly generated grains, in which the opposite sign of DMI coefficients are assigned (b). (c) The relaxed ground state spin texture, where spatial shift of the helical vector is observed. The simulation window is  $1024 \times 1024 \text{ nm}^2$ .

Finally, we perform electron energy loss spectroscopy (EELS) to uncover the underlying chemical compositions in our structures (Fig. 7) and to investigate the apparent discrepancy between substrate-induced stress and the orientation of the helical vector. As noted above, our observation of helical phases suggests a lack of substrate-induced strain, which could be explained if the FeGe film has been released from the underlying Si during sample preparation. From our EELS analysis, we find that regions with helical states show no chemical signature of Si, here the sample is only FeGe, and the silicon substrate has been polished away. However, regions of FeGe supported by Si show no in-plane Q helical states. This finding states that it is easier to observe in-plane helical phases in regions of supported by only FeGe; here, the sample is thinner, due to the way plan-view samples are prepared, and the FeGe film is released from substrate-induced strain. Regions of FeGe supported by Si tend to be thicker ( $<176 \text{ nm}$ ), which would make it more difficult, but not impossible to observe the Lorentz deflection from the helical phases. The lack of magnetic contrast (data not shown) suggests that the substrate-induced strain of Si on the FeGe affects the rotation of the Q vectors so that few or any of the vectors are aligned in-plane.

This is an important confirmation about the nature of magnetic phases in epitaxial B20 phases, and it is consistent with our expectation discussed in Sec. IV, previous neutron scattering



experiments[12,51-53] and FMR experiments conducted on sputtered FeGe films. We note that because skyrmions emerge only from the helical states with an in-plane  $Q$  vector, it is inconsistent with experiments that interpret an “extra” contribution to the Hall effect – widely interpreted as a purely topological hall effect and ignoring other possible sources – as evidence of a skyrmion phase in sputtered FeGe on Si [4,54]. Here, we show that suspended FeGe films can stabilize in-plane helices, therefore, we assert that magnetic skyrmions can be realized in these suspended films as in the single crystal FeGe. However, FeGe films on Si substrate have easy-plane anisotropy that may prevent skyrmion formation[52].

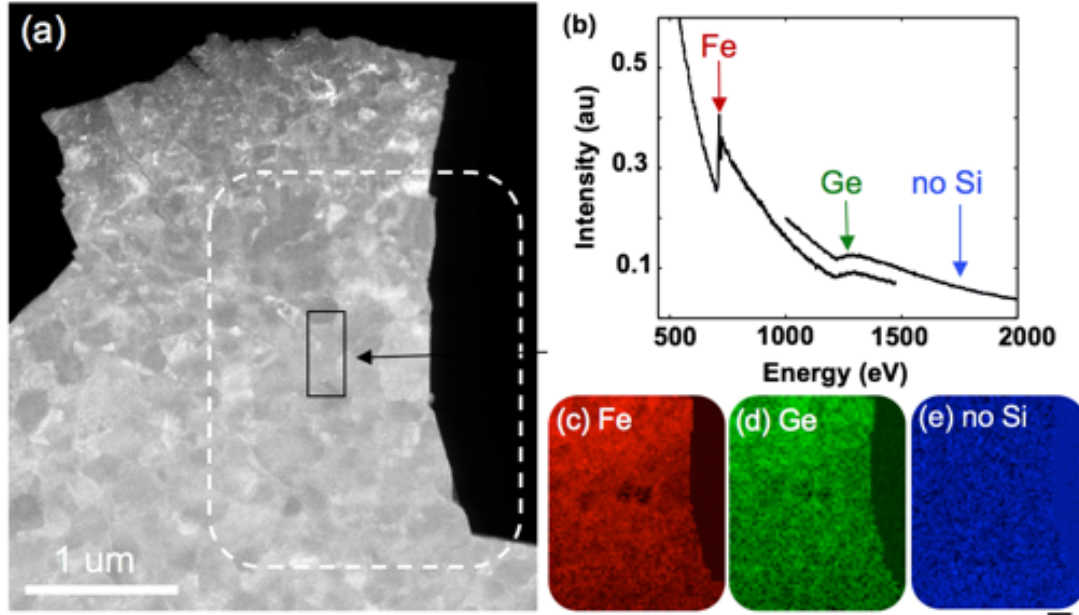


FIG. 7. We find that magnetic images only occur in free-standing FeGe, when we perform electron energy loss spectroscopy (EELS). (a) The ADF image shows the region where the EELS has been recorded. (b) Shows the Fe-L edge and Ge-L edge spectra recorded in dual-EELS mode from the region marked by the small black box. The Si-K edge is not detectable. EELS maps from the white dashed region for (c) Fe, (d) Ge and (e) Si. Here the Si underneath the sputtered FeGe has been completely removed such that the FeGe is free-standing. Black scale bar underneath (e) is 200 nm corresponding to images (c-e).

## VII. Conclusion

In this paper, we provide three themes: (1) we quantify the sensitivity of an electron beam deflection in LSTEM and its dependence on the number of electrons and pixels on the detector, (2) we find having a high dynamic range detector is essential when measuring small electromagnetic fields, and (3) we show how we can effectively use all the scattering information from the CBED pattern collected by the EMPAD to disentangle magnetic and grain contrasts from each other. Decoupling them together enables an approach for efficient Lorentz imaging of magnetic samples simultaneously with grain structure, and, investigations of changes in the magnetic field from crystal structures at the nanometer scale. We believe that our approach is important in the characterization of real devices where small changes in grain structure can be critical to device performance.

More systematically, we find that the sensitivity in magnetic field detection is more dependent on the number of electron than on the number of pixels in our detector, where high dynamic range detectors are a necessity when imaging  $\mu\text{T}$ -level magnetic fields. Whereas, having more pixels in our detector becomes important when we decouple signals from magnetic and grain contrast. Here, we filter long-range (magnetic contrast) and short-range (grain contrast) potentials using our acquired CBED pattern for thin film sputtered B20 FeGe on Si. We observed a shift in the helical vectors as it glides between grain structures. By performing micromagnetic simulations, we generate random grain orientations and signs of DMI. From these simulations, we observed that the DMI is coupled to the crystal chirality, which can dictate how the helical vectors change when going in between grains. Our technique can also be applied to other chiral magnets. Here, understanding the nanoscale physical and magnetic properties of chiral magnetic materials is key to advancing next generation magnetically-driven devices.

**ACKNOWLEDGMENTS** Electron microscopy experiments of thin-film FeGe samples and equipment were supported by the Cornell Center for Materials Research, through the National Science Foundation MRSEC program, award DMR 1719875. Electron microscopy measurements of single-crystal FeGe samples were supported by DARPA under cooperative agreement D18AC00009. Thin-film FeGe growth and micromagnetic modeling were supported by the Department of Energy Office of Science under grant No. DE-SC0012245. Growth of single-crystal FeGe was made by M.J.S. and S. J., who are supported by NSF grant ECCS-1609585. M.J.S. also acknowledges support from the NSF Graduate Research Fellowship Program grant number DGE-1256259.

## Appendix A: Determining Magnetic Field Detection Sensitivity: Analytical Model

How sensitive the measurement for magnetic field using center of mass (COM) imaging depends on how well we can track the deflection of the electron beam. To quantify this, we follow an analytical approach to determine the accuracy of the magnetic field using a model previously described by Chapman et al. [19,27]. In this analytical model, the sensitivity of our signal has two dependencies: (1)  $\alpha$ , the semi-convergence angle of the electron beam, which provides the limit in spatial resolution, and (2)  $n$ , the number of electrons or dose of the electron beam, which corresponds to the number of electrons needed to sustain a signal that is adequately above Poisson noise. From Chapman et al., the signal  $S$  is the difference in intensity over the entire detector, described as:

$$S = \frac{4\beta_L}{\pi\alpha} \quad (\text{A1})$$

where  $\beta_L$  corresponds to the deflection angle of the electron beam from the local magnetic field of the sample. Here, the dose  $n$  is

$$n = B\pi^2\alpha^2 D^2\tau / 4e \quad (\text{A2}),$$

where  $B$  is the brightness of the electron gun,  $D$  is the beam diameter, and  $\tau$  is the time interval. The signal with respect to the dose is  $S * n$ , and the noise due to Poisson statistics is  $\sqrt{n}$ . We calculate the signal to noise ratio (SNR) as  $s = S * \sqrt{n}$ . To estimate the standard deviation of the noise, we set  $s = 1$ , and rewrite the equation in terms of the minimum deflection angle,  $\beta_L$ ,



$$\beta_L = \pi\alpha / 4 \sqrt{n} \quad (\text{A3}).$$

Here, we add a time dependence to Equation A3 to compare the field resolution needed in the electron microscope to other magnetic imaging techniques such as superconducting quantum interference device (SQUID) and nitrogen vacancy (NV) centers[29], we get the minimum deflection  $\beta_L$  in terms  $1/\sqrt{Hz}$ , as:

$$\beta_t = \beta_L \sqrt{\tau} \quad (\text{A4}),$$

where  $\tau$  is the acquisition time in seconds.

## Appendix B: Determining Magnetic Field Detection Sensitivity: Numerical Model

In our numerical simulation, we assume a one-dimensional detector, represented as the vector form of  $\vec{v}$ . Our detector,  $\vec{v}$ , is then entirely illuminated by an electron beam represented by a Gaussian distribution,  $g_j$  [Fig. B1(a)], which is equal to the  $j$  size of our detector. Each index of  $\vec{v}$  is the number of pixels on the detector, which changes in size by  $j$ , where  $v_j = [1:j]$ . The width of the detector based on its  $j$  size is  $w_j = \frac{j}{2}$ . The center pixel of the detector,  $\vec{v}$ , is  $c_j = \frac{j+1}{2}$ .

Mathematically, our gaussian distribution becomes  $g_j = \frac{1}{\sqrt{2\pi w_j^2}} e^{-\frac{(v_j - c_j)^2}{2w_j^2}}$ , using all the variables that we have previously defined.

To make our Gaussian distribution into an ideal electron beam probe with an electron dose, we multiply our Gaussian,  $g_j$ , with the number of electrons,  $n_i$ , as:  $g_{ij} = n_i * g_j$ . Here, the total number of electrons,  $n$ , changes with  $i$  number of electrons =  $n_i$ .

However, real electron probes have variations. Therefore, to reflect a real electron probe, we added Poisson noise on top of our Gaussian distribution. To get statistics from the Poisson noise, we ran  $k$  number of samples on our Gaussian distribution with different Poisson noise,  $p_{kij}$ . We get various shapes to our probe [Fig. B1(b)]. From which, the total number of  $k$  samples is represented as  $N$ .

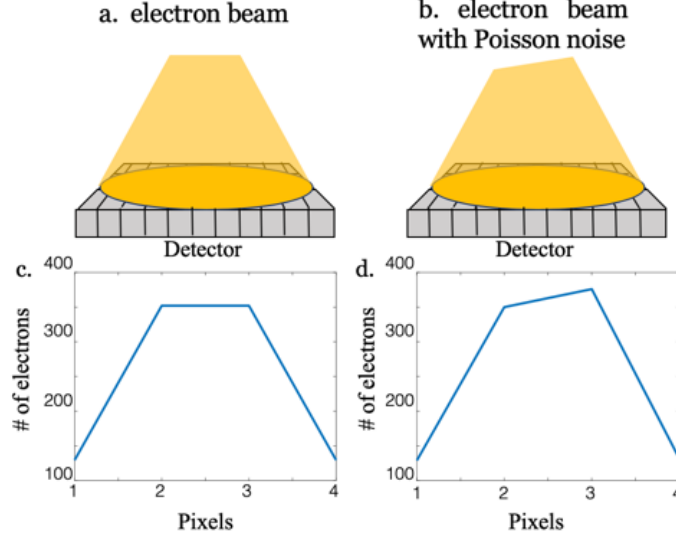


FIG. B1. Simulated Electron Probe for a One-Dimensional Pixel Detector. Schematic and line profile of an ideal Gaussian  $g$  shown in (a), (c) on a detector with a discrete number of pixels. Similarly, when we have an ideal Gaussian with Poisson noise, we can represent this as a real electron source on a detector with finite number of pixels, schematic and line profile shown in (b), (d).

Using our model, we calculate the COM,  $\mu_{ijk}$ , as

$$\mu_{ijk} = \sum_{k=1}^{\# \text{ of samples}} \sum_{i=1}^{\# \text{ of electrons}} \sum_{j=2}^{\text{size of detector}} \frac{p_{kij} * v_j}{n_i * g_{ij}} \quad (\text{B1}).$$

Assuming that the detector is the  $j$  size and the electron beam has  $i$  number of electrons, we can reduce our equation down to only a summation of  $k$ , the number of times we run COM calculations. Here, for each  $k$  sample, the Poisson noise on top of Gaussian electron probe and detector is unique [Fig. B1(d)]. The reduced COM is represented as:

$$\mu_k = \sum_{k=1}^{\# \text{ of samples}} \frac{p_k * \vec{v}}{n * g} \quad (\text{B2}).$$

Here,  $\mu_k$  represents the COM on our detector,  $\vec{v}$ , in units of pixels. We find the mean,  $\bar{\mu}$ , from all  $N$  samples of  $\mu_k$  as

$$\bar{\mu} = \frac{\sum_{k=1}^{\# \text{ of samples}} \mu_k}{N} \quad (\text{B3}).$$

Using Equation B2 and B3, we calculate the standard deviation,  $\sigma_k$ , as

$$\sigma_k = \sqrt{\frac{1}{N-1} \sum_{k=1}^N (\mu_k - \bar{\mu})^2} \quad (\text{B4})$$

We perform a normalization for  $\sigma_k$ , with respect to the number of pixels in our detector, as

$$\sigma_{norm} = \frac{\sigma_k}{v} \quad (B5),$$

where  $v$  represents the total number of pixels in the detector,  $\vec{v}$ . The normalization of  $\sigma_k$  is important because as the number of pixels increase on our detector, the area on our detector that is illuminated by the beam stays the same. Therefore, as pixel number is increase, the size of each pixel relative to the size of the electron beam is reduced. To counteract this effect, we must normalize  $\sigma_k$  by the total number of pixels on our detector to keep the weights for each pixel the same as we increase the number of pixels.

Using the relation between SNR and standard deviation, we can get our SNR as

$$SNR = \frac{1}{\sigma_{norm}} \quad (B6).$$

Then, we relate our  $\sigma_{norm}$  back to the minimum deflection angle observed and convert our  $\sigma_{norm}$  to the minimum deflection as

$$\beta = \sigma_{norm} * \alpha \quad (B7)$$

where  $\beta$  is the minimum deflection angle and  $\alpha$  is the full convergence angle of our electron beam. Here, we can observe how each variable change when we vary the number of electrons,  $n$ , and the number of pixels on our detector,  $\vec{v}$ . We used  $N = 2000$  samples for all our simulations.

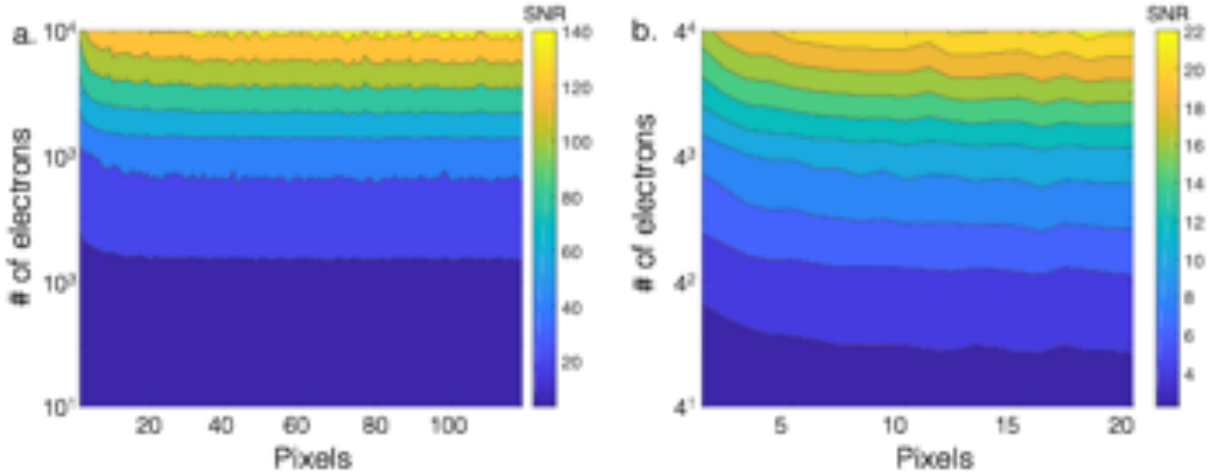


FIG. B2. SNR dependence (a) on the number of electrons and pixels on the detector and for (b) low numbers of electrons and pixels on our detector. We realized that no matter how many pixels is added to our detector, if the number of electrons remain under 16, the SNR will remain under 5.

In Fig. B2, we analyze how SNR is dependent on the number of electrons and pixels on our detector. From Fig. B2(a), if the value for SNR is above Rose's criterion  $\sim 5$  [49], our SNR is adequate for detecting small deflection angles or small magnetic fields. In addition, in FIG B2(a), we find that SNR is much more dependent on the number of electrons in our beam than it is on the number of pixels on our detector. In fact, when we reduce the number of pixels and electrons such that the two numbers are comparable in scale [Fig. B2(b)], we observe that the SNR is still

dependent on the number of electrons than the number of pixels. We find that our SNR remains below 5 when the number of electrons is less than 16, no matter how many pixels we have in our detector.

#### References:

- [1] S. Emori, U. Bauer, S. M. Ahn, E. Martinez, and G. S. Beach, *Nat Mater* **12**, 611 (2013).
- [2] A. Fert, V. Cros, and J. Sampaio, *Nat Nanotechnol* **8**, 152 (2013).
- [3] S. Y. Huang, X. Fan, D. Qu, Y. P. Chen, W. G. Wang, J. Wu, T. Y. Chen, J. Q. Xiao, and C. L. Chien, *Physical Review Letters* **109**, 107204 (2012).
- [4] S. X. Huang and C. L. Chien, *Phys Rev Lett* **108**, 267201 (2012).
- [5] A. Hrabec, N. A. Porter, A. Wells, M. J. Benitez, G. Burnell, S. McVitie, D. McGrouther, T. A. Moore, and C. H. Marrows, *Physical Review B* **90**, 020402(R) (2014).
- [6] X. Z. Yu, Y. Onose, N. Kanazawa, J. H. Park, J. H. Han, Y. Matsui, N. Nagaosa, and Y. Tokura, *Nature* **465**, 901 (2010).
- [7] S. Muhlbauer, B. Binz, F. Jonietz, C. Pfleiderer, A. Rosch, A. Neubauer, R. Georgii, and P. Boni, *Science* **323**, 915 (2009).
- [8] T. Schulz *et al.*, *Nat Phys* **8**, 301 (2012).
- [9] I. Dzyaloshinsky, *J Phys Chem Solids* **4**, 241 (1958).
- [10] T. Moriya, *Phys Rev* **120**, 91 (1960).
- [11] E. Turgut, A. Park, K. Nguyen, A. Moehle, D. A. Muller, and G. D. Fuchs, *Physical Review B* **95**, 134416 (2017).
- [12] N. A. Porter, C. S. Spencer, R. C. Temple, C. J. Kinane, T. R. Charlton, S. Langridge, and C. H. Marrows, *Physical Review B* **92**, 144402 (2015).
- [13] N. Nagaosa and Y. Tokura, *Nat Nanotechnol* **8**, 899 (2013).
- [14] X. Z. Yu, N. Kanazawa, Y. Onose, K. Kimoto, W. Z. Zhang, S. Ishiwata, Y. Matsui, and Y. Tokura, *Nature Materials* **10**, 106 (2010).
- [15] Y. F. Li, N. Kanazawa, X. Z. Yu, F. Kagawa, and Y. Tokura, *Physical Review Letters* **112**, 059702 (2014).
- [16] Y. F. Li, N. Kanazawa, X. Z. Yu, A. Tsukazaki, M. Kawasaki, M. Ichikawa, X. F. Jin, F. Kagawa, and Y. Tokura, *Physical Review Letters* **110**, 117202 (2013).
- [17] T. L. Monchesky, J. C. Loudon, M. D. Robertson, and A. N. Bogdanov, *Physical Review Letters* **112**, 059701 (2014).
- [18] E. M. Waddell and J. N. Chapman, *Optik* **54**, 83 (1979).
- [19] J. N. Chapman, E. M. Waddell, P. E. Batson, and R. P. Ferrier, *Ultramicroscopy* **4**, 283 (1979).
- [20] T. Matsumoto, Y. G. So, Y. Kohno, H. Sawada, R. Ishikawa, Y. Ikuhara, and N. Shibata, *Sci Rep* **6**, 35880 (2016).
- [21] D. McGrouther, Lamb, R. J., Krajnak, M., McFadzean, S., McVitie, S., Stamps, R. L., Leonov, A. O., Bogdanov, A. N., Togawa Y., *New Journal of Physics* **18**, 12 (2016).
- [22] A. Lubk and J. Zweck, *Phys Rev A* **91**, 023805 (2015).
- [23] R. Close, Z. Chen, N. Shibata, and S. D. Findlay, *Ultramicroscopy* **159**, 124 (2015).
- [24] K. Muller *et al.*, *Nat Commun* **5**, 5653 (2014).
- [25] M. W. Tate *et al.*, *Microsc Microanal* **22**, 237 (2016).
- [26] J. N. Chapman, *J Phys D Appl Phys* **17**, 623 (1984).

- [27] J. N. Chapman, Batson, P. E., Waddell, E. M., Ferrier, R. P. , Ultramicroscopy **3**, 203 (1978).
- [28] P. Ehrenfest and P. S. Epstein, Proc Natl Acad Sci U S A **13**, 400 (1927).
- [29] S. Hong, M. S. Grinolds, L. M. Pham, D. Le Sage, L. Luan, R. L. Walsworth, and A. Yacoby, Mrs Bull **38**, 155 (2013).
- [30] D. S. Song *et al.*, Physical Review Letters **120**, 167204 (2018).
- [31] F. S. Zheng *et al.*, Physical Review Letters **119**, 197205 (2017).
- [32] F. S. Zheng *et al.*, Nature Nanotechnology **13**, 451 (2018).
- [33] E. Turgut, M. J. Stolt, S. Jin, and G. D. Fuchs, J Appl Phys **122**, 183902 (2017).
- [34] S. Schneider *et al.*, Physical Review Letters **120**, 217201 (2018).
- [35] M. J. Stolt, S. Schneider, N. Mathur, M. J. Shearer, B. Rellinghaus, K. Nielsch, and S. Jin, Adv Funct Mater **29**, 1805418 (2019).
- [36] M. J. Stolt, X. Sigelko, N. Mathur, and S. Jin, Chem Mater **30**, 1146 (2018).
- [37] S. X. Huang and C. L. Chien, Phys Rev Lett **108**, 267201 (2012).
- [38] N. A. Porter, J. C. Gartside, and C. H. Marrows, Physical Review B **90**, 024403 (2014).
- [39] J. C. Gallagher, K. Y. Meng, J. T. Brangham, H. L. Wang, B. D. Esser, D. W. McComb, and F. Y. Yang, Phys Rev Lett **118**, 027201 (2017).
- [40] A. S. Ahmed, J. Rowland, B. D. Esser, S. R. Dunsiger, D. W. McComb, M. Randeria, and R. K. Kawakami, Phys Rev Mater **2**, 041401(R) (2018).
- [41] J. N. Chapman, I. R. Mcfadyen, and S. Mcvitie, Ieee T Magn **26**, 1506 (1990).
- [42] S. Majert and H. Kohl, Ultramicroscopy **148**, 81 (2015).
- [43] M. Krajnak, D. McGrouther, D. Maneuski, V. O'Shea, and S. McVitie, Ultramicroscopy **165**, 42 (2016).
- [44] M. C. Cao, Y. M. Han, Z. Chen, Y. Jiang, K. X. Nguyen, E. Turgut, G. D. Fuchs, and D. A. Muller, Microscopy-Jpn **67** (2018).
- [45] W. J. Chen, Y. Zheng, and B. Wang, Sci Rep **5**, 11165 (2015).
- [46] Y. Nii *et al.*, Nat Commun **6**, 8539 (2015).
- [47] S. L. Zhang *et al.*, Sci Rep-Uk **7**, 123 (2017).
- [48] C. S. Spencer *et al.*, Physical Review B **97**, 214406 (2018).
- [49] A. Rose, *Vision: Human and Electronic* (Plenum Press, 1973).
- [50] A. Vansteenkiste, J. Leliaert, M. Dvornik, M. Helsen, F. Garcia-Sanchez, and B. Van Waeyenberge, Aip Adv **4**, 107133 (2014).
- [51] E. A. Karhu, U. K. Rossler, A. N. Bogdanov, S. Kahwaji, B. J. Kirby, H. Fritzsche, M. D. Robertson, C. F. Majkrzak, and T. L. Monchesky, Physical Review B **85**, 094429 (2012).
- [52] M. N. Wilson, A. B. Butenko, A. N. Bogdanov, and T. L. Monchesky, Physical Review B **89**, 094411 (2014).
- [53] M. N. Wilson, E. A. Karhu, D. P. Lake, A. S. Quigley, S. Meynell, A. N. Bogdanov, H. Fritzsche, U. K. Rossler, and T. L. Monchesky, Physical Review B **88**, 214420 (2013).
- [54] J. C. Gallagher, K. Y. Meng, J. T. Brangham, H. L. Wang, B. D. Esser, D. W. McComb, and F. Y. Yang, Phys Rev Lett **118**, 027201 (2017).